

# Reconfigurable Organic Electrochemical Transistors with High Dynamic Ranges for Fully Integrated Physical Reservoir Computing

Chunghi Han, Mingyu Kim, Seong Jun Park, Jung Sun Eo, Donghyeok Kim, Young Ran Park, Sungjune Jung,\* and Gunuk Wang\*

Reconfigurable organic electrochemical transistors (r-OECTs) are considered a promising platform for fully integrated physical reservoir computing (RC) owing to their dual switching modes, which are suitable for both the reservoir and readout layers. However, their restricted dynamic ranges (DR) have constrained their nonlinearity, high-dimensional mapping capacity, and the reconfigurability of neural networks for optimal physical RC. In this study, r-OECTs with a modified PEDOT:PSS channel and solid electrolyte is designed and fabricated, achieving dual-modal essential synaptic functions (nonvolatile and volatile) through ethylene glycol (EG) content adjustment. The r-OECTs with the EG of 680 and 1000  $\mu\text{L}$  exhibit exceptional DR of  $1.12 \times 10^5$  in nonvolatile mode and  $1.20 \times 10^3$  volatile mode, respectively, representing a significant improvement over previously reported OECTs. The nonvolatile mode exhibits long-term memory with robust and gradual long-term potentiation (LTP) and long-term depression (LTD), while the volatile mode demonstrates short-term memory for extracting reservoir states. The r-OECTs, functioning in two modes as the reservoir and readout layers with high DRs, enable accurate classification of human activities such as jogging (J), brushing teeth (B), and folding clothes (F) with an accuracy of 84.38% in a fully integrated physical RC system.

## 1. Introduction

The world is awash in a sea of time-series data. From the minute fluctuations in our dynamic body and organ movements captured

by sensors to the global shifts in weather patterns tracked by satellites, we are constantly generating and collecting information that unfolds over time.<sup>[1]</sup> This data, propelled by a dynamic process, contains invaluable insights into the behavior of individuals, systems, and the surrounding world. This plays a vital role in diverse fields including personal health monitoring,<sup>[2]</sup> financial markets,<sup>[3]</sup> and environmental monitoring analysis.<sup>[4]</sup> By analyzing these temporal patterns, we can unlock a deeper understanding of how things change, predict future events, and make more informed decisions.<sup>[5]</sup>

Among various analyzing methods, artificial intelligence (AI) has become a crucial tool for deriving valuable insights from the continuously expanding volume of time-series data.<sup>[6]</sup> Diverse AI methodologies, including recurrent neural networks (RNN),<sup>[7]</sup> long short-term memory (LSTM) networks,<sup>[8]</sup> and convolutional neural networks (CNNs),<sup>[9]</sup> have demonstrated efficacy in capturing temporal dependencies

and generating precise predictions of time-series data. Nevertheless, the growing influx of time-series data necessitates substantial computational resources for these methods, imposing a strain on the implementation of the artificial neural networks (ANNs) hardware.<sup>[10]</sup>

From this perspective, physical reservoir computing (RC) has shown limelight as a prominent alternative for processing time-series data due to its intrinsic efficiency and simplicity, which can be easily applied in physical ANNs.<sup>[11]</sup> Unlike traditional RNN, where all connection weights are trained, reservoir computing utilizes a fixed, random network to transform the input signal over time into a high-dimensional and non-linear state space.<sup>[12]</sup> Only a simple readout layer is trained to map this reservoir state to the desired output. This approach significantly reduces the training complexity and makes it suitable for the implementation of physical device system.<sup>[13]</sup> Various device types for the physical RC system have been demonstrated to date.<sup>[14–16]</sup> Recently, Zhong et al. reported the parallel RC system utilizing a single Ti/TiO<sub>x</sub>/TaO<sub>x</sub>/Pt memristor with a simple mask process, processing temporal signals such as waveform classification and spoken-digit recognition with low operating power.<sup>[17]</sup> Shi et al.

C. Han, M. Kim, J. S. Eo, D. Kim, Y. R. Park, G. Wang  
KU-KIST Graduate School of Converging Science & Technology  
Korea University  
Seoul 02841, Republic of Korea  
E-mail: [gunukwang@korea.ac.kr](mailto:gunukwang@korea.ac.kr)

S. J. Park, S. Jung  
Department of Materials Science and Engineering  
Pohang University of Science and Technology (POSTECH)  
67 Cheongam-Ro, Nam-Gu, Pohang 37673, Republic of Korea  
E-mail: [sjjung@postech.ac.kr](mailto:sjjung@postech.ac.kr)

G. Wang  
Department of Integrative Energy Engineering  
Korea University  
Seoul 02841, Republic of Korea

The ORCID identification number(s) for the author(s) of this article can be found under <https://doi.org/10.1002/adfm.202423814>

DOI: 10.1002/adfm.202423814

demonstrated an antiferroelectric field-effect transistor-based RC system utilizing a light-sensitive  $\text{MoS}_2$  channel, facilitating adjustable temporal dynamics under electrical and optical stimuli to enhance reservoir states.<sup>[18]</sup> We have also developed a wide reservoir computing system based on a multilayered 3D stacked  $\text{WO}_x$  memristive crossbar array for efficient learning and forecasting of multiple time-series data.<sup>[19]</sup>

Although these proposed physical reservoir computing systems are noteworthy, most focus on only the execution of the reservoir layer leveraged by their short-term and nonlinear switching characteristics. In contrast, the readout layer has been primarily processed using a software-driven learning algorithm based on conventional computing resources. Those hybrid RC systems, while promising, suffer from significant drawbacks due to their reliance on external software for readout. These systems require signal conversion devices and complex circuitry to bridge the gap between the physical reservoir and the software, leading to increased system size and reduced integration potential.<sup>[20,21]</sup> The necessary signal processing steps can introduce data distortion and time delays, compromising both reliability and real-time performance. Furthermore, the limited parallelism inherent in these hybrid systems, compared to the inherent parallelism of physical devices, hinders their ability to efficiently process large datasets and significantly increases energy consumption. These limitations are particularly detrimental for resource-constrained applications such as edge-computing devices and embedded in-sensor computing, where real-time processing, low power consumption, miniaturization, and high reliability are paramount. These challenges underscore the importance of developing fully integrated physical RC systems where both the reservoir and readout layers are implemented through a single physical device framework. This approach can lead to more compact, energy-efficient, and adaptable RC systems suitable for a wide range of applications.<sup>[21]</sup>

Organic electrochemical transistors (OECTs), which utilize an electrolyte as a gate insulator and an organic mixed ionic-electronic conductor (OMIEC), have emerged as promising candidates for implementing RC in physical device platforms.<sup>[22–24]</sup> They function at low voltages via ion-based conduction and provide high short-term transconductance due to charged ion movements between the channel and electrolyte, enabling the efficient transformation of chemical signals into electrical signals.<sup>[25]</sup> These distinctive characteristics make them particularly suitable for the establishment of the physical RC.<sup>[26]</sup> For example, Cucchi et al. presented nonlinear and dendritic fiber-formed networks of OECTs for producing semi-random networks as reservoirs, enabling a rich variety of responses of time-dependent electrical excitations.<sup>[26]</sup> Liu et al. fabricated a scalable and stretchable micro-OECTs array and adopted them as RC framework for wearable integrated and soft electronic (WISE) platform.<sup>[27]</sup>

In addition to the utilization of the switching property in OECTs, such as in only reservoir or volatile switching layer, recently, its dual-modal memory functions by different magnitudes of input sequences have been suggested for the application of both reservoir (or volatile) and readout (nonvolatile synapse) layers.<sup>[28–33]</sup> Yin et al. demonstrated dual-modal switching characteristics by manipulating pulse voltage and duration, utilizing these properties in a fully-OECT reservoir computing system.<sup>[31]</sup> Wang et al. developed a multifunctional OECT that

can be selectively doped by ions by the adjustment of the gate voltages, facilitating reconfigurable functionality as a volatile receptor and nonvolatile synapse for the realization of a homogeneous sensing-processing integrated system.<sup>[32]</sup> Similar to above OECTs, Liu et al. developed a high-density organic ion-gated transistor (OIGT) utilizing a modified photolithography technique, demonstrating its capability to be reconfigured via gate voltage between volatile and nonvolatile modes, which are appropriate for constructing RC.<sup>[33]</sup>

To further enhance the performance of a physical RC system based on OECTs, however, it is essential to optimize the nonlinearity and high-dimensional mapping capacity of the reservoir.<sup>[19]</sup> These characteristics are strongly influenced by the dynamic range (DR) of the OECTs, which dictates the range of accessible conductance states, and their switching behavior.<sup>[19,34]</sup> A broader DR allows the reservoir to capture a wider spectrum of input signal variations and perform richer nonlinear transformations, effectively expanding the reservoir's state space and enhancing its ability to represent complex temporal patterns. Moreover, an extensive DR of the readout device nodes could also augment the number of multi-states, thereby enhancing the reconfigurability of neural networks.<sup>[35,36]</sup> These factors contribute to improving both pattern recognition accuracy and the overall computational capability of the physical RC system. However, the DRs of prior OECT devices for physical RC systems are relatively smaller as compared to other switching devices regardless for the applications of reservoir and readout layer so far,<sup>[16,37–39]</sup> which is insufficient for achieving high-dimensional mapping of input signals and the updating capability. In this point of view, it is essential to design OECT devices with reconfigurable switching features along with high DR values for both the reservoir and readout layers in physical RC.

Here, we explore the potential of reconfigurable OECTs (r-OECTs) as both reservoir and readout layers for implementing a fully integrated physical RC system. The r-OECTs, based on a modified PEDOT:PSS channel and the solid electrolyte of ([EMIM<sup>+</sup>][EtSO<sub>4</sub><sup>−</sup>]), are designed to achieve dual-modal switching characteristics with high DRs. By modifying the morphology of the PEDOT:PSS film through adjustments to the ethylene glycol (EG) contents, the r-OECTs can operate in controllable non-volatile and volatile modes, each demonstrating a high DR that surpasses that of previously reported r-OECTs. The transient responses of both modes under various gate pulse conditions for the implementation of the readout and reservoir layers for physical RC are analyzed, effectively showcasing robust LTP and LTD functions in the nonvolatile mode, as well as distinct reservoir states in the volatile mode, respectively. Our r-OECTs-based reservoir computing can classify time-series human activities with an accuracy of 84.38%, highlighting their potential for the hardware implementation of a fully integrated physical RC.

## 2. Results and Discussion

**Figure 1a** illustrates the schematic representation of a r-OECT fabricated on a  $\text{SiO}_2/\text{p}^{++}\text{Si}$  substrate. This device features a top-gate configuration with a probe tip connected to the solid electrolyte (SE) and a lateral channel structure, comprising deposited Al/Au source (S) and drain (D) electrodes and a patterned p-type PEDOT channel on the substrate. The Poly

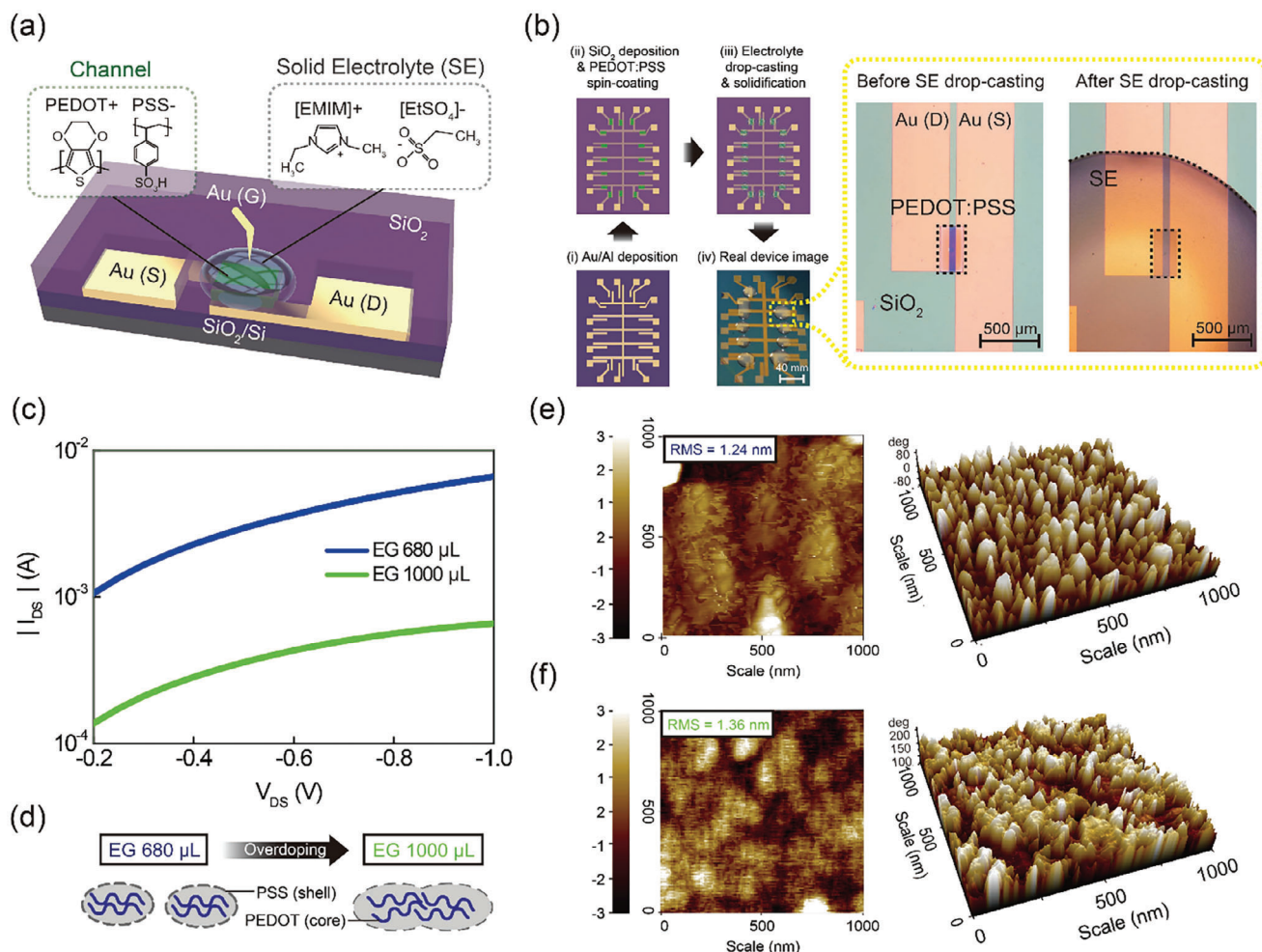


**Figure 1.** a) Schematic illustration of the r-OECT device consisting of PEDOT:PSS channel and the SE of [EMIM]<sup>+</sup>[EtSO<sub>4</sub>]<sup>-</sup>. b) Fabrication process for the r-OECT device (scale bar, 40 nm). The yellow box shows top-view optical microscope images of r-OECT before and after SE drop-casting (scale bar, 500 μm). c) I<sub>DS</sub>-V<sub>DS</sub> curves of the OECT devices with EG contents of 680 and 1000 μL, respectively. d) Schematics of PEDOT:PSS doped with different EG contents of 680 and 1000 μL, respectively. e, f) AFM 2D height and 3D phase images of PEDOT:PSS coated on SiO<sub>2</sub>/Si substrate with EG contents of 680 and 1000 μL, respectively.

(3,4-ethylenedioxythiophene):poly(styrenesulfonate) layer, consisting of the conductive polymer poly(3,4-ethylenedioxythiophene) (PEDOT) complexed with polystyrene sulfonate (PSS) as a counter-ion, thereby PEDOT wrapped in PSS shell carries hole charges (green dashed box in Figure 1a).<sup>[40]</sup> The PEDOT:PSS is recognized for its high electrical conductivity and notable film stability in electrolyte contact, which benefits electronic applications in OECTs.<sup>[41]</sup> The SE is synthesized from ionic liquid, 1-ethyl-3-methylimidazolium ethyl sulfate ([EMIM]<sup>+</sup>[EtSO<sub>4</sub>]<sup>-</sup>) and subsequently combined with poly(*N*-isopropylacrylamide) (Poly-NIPAm), as shown in the gray dashed box in Figure 1a. Typically, the NIPAm monomers undergo free-radical polymerization, transitioning to Poly-NIPAm, which facilitates rapid solidification of the SE.<sup>[42]</sup> Detailed preparation of the PEDOT:PSS channel and SE are illustrated in the (see Figures S1 and S2, Supporting Information). Figure 1b shows the fabrication steps for the r-OECT devices. The patterned Au/Al metals were fabricated through photolithography and thermal evaporation, and utilized in S and D electrodes for the

r-OECT devices (i) of Figure 1b). This device design allows the integration of 16 r-OECT devices in a single substrate (1.5 × 2.0 cm<sup>2</sup>), facilitating both shared and distinct gating configurations. To define each channel area of the r-OECT devices and reveal contact pads, a SiO<sub>2</sub> layer was deposited using radio frequency (RF) sputtering under condition of CF<sub>4</sub> at 40 sccm and O<sub>2</sub> at 4 sccm, subsequently followed by the reactive ion etching (RIE) process to selectively eliminate SiO<sub>2</sub> from the channel and contact pad regions after the photolithography process (ii) of Figure 1b). This process also allows the isolation of the SE from the contact S and D pads, thereby minimizing electrical interference. To form the channel, a pre-synthesized PEDOT:PSS was spin-coated and baked on the patterned devices, followed by the lift-off process of the patterned photoresistor (iii) of Figure 1b). The channel dimensions used in this study are 45 and 55 μm in length, 200 μm in width, and 104 nm in thickness. Note that the thickness of the PEDOT:PSS channel was measured by Dektak-XT stylus profilometer (see Figure S3, Supporting Information). Then, the prepared liquid electrolyte is drop-cast



selectively over the channel area and subsequently solidified under UV exposure to form the SE (iv) of Figure 1b). The SE appears as opaque droplets with diameters ranging from  $\approx 15$ –30 nm, onto which gating is applied via Au probe tip, as shown in the right of Figure 1b.

Generally, the conductance of the PEDOT:PSS film is influenced by the complex interplay of the morphological factors, including the film morphology, PEDOT domain size, and the boundaries of the PSS shell.<sup>[43–45]</sup> Moreover, they may influence the migration extent of cations from the SE, thereby impacting the electrical properties.<sup>[46]</sup> In this context, the ethylene glycol (EG) content has the potential to significantly modify the film morphology, which could be used to reconfigure the switching characteristics of the OECT devices.<sup>[47,48]</sup> When a proper amount of EG contents is incorporated into the pristine PEDOT:PSS, composed of ellipsoidal grains with a PEDOT (core) and PSS (shell) structure, EG rearranges the PEDOT chains from a coil-like to a linear form, thinning the PSS boundary and promoting crystallization, which enlarges the grain size.<sup>[49,50]</sup> This process facilitates carrier mobility between PEDOT chains, increasing carrier concentration and thus the conductivity of the channel. However, when the excessive amount of EG content is incorporated into the pristine PEDOT:PSS, the PSS shell becomes almost entirely removed, leading to grain enlargement and overlapping, resulting in clustering of PEDOT chains.<sup>[49]</sup> Consequently, the linear structure of PEDOT chains becomes entangled, reducing conductivity in the channel. Figure 1c shows the drain-source current ( $I_{DS}$ ) as a function of the drain-source voltage ( $V_{DS}$ ) for varying amount of EG contents in the PEDOT:PSS channel of the OECT devices (see also Figure S4, Supporting Information).<sup>[48,49]</sup> Note that the conductance with different gate voltage ( $V_G$ ) for varying amount of EG contents (0, 680, and 1000  $\mu\text{L}$ ) in the PEDOT:PSS channel is investigated (see Figure S5, Supporting Information). When adding EG of 680  $\mu\text{L}$  in the PEDOT:PSS film, the  $I_{DS}$  of the OECT device is greater than that of EG = 0, whereas the  $I_{DS}$  of EG 1000  $\mu\text{L}$  is lower. This is due to the modification of PEDOT chains and PSS shells depending on the amount of EG content, as previously mentioned, as shown in Figure 1d and Figure S5. Figure 1e,f present the atomic force microscope (AFM) 2D height images and 3D phase images of PEDOT:PSS films coated on a  $\text{SiO}_2/\text{Si}$  substrate with 680 and 1000  $\mu\text{L}$  of EG, respectively. The surface root mean square (RMS) roughness slightly increases from 1.24 to 1.36 nm as the EG increases from 680 to 1000  $\mu\text{L}$ , which indicates the increase in surface irregularity. Furthermore, for 1000  $\mu\text{L}$  of EG, the bright areas associated with PEDOT-rich (greater height) become intertwined, while the dim areas representing PSS-rich diminish its height.<sup>[51]</sup> Additional material characterization for the PEDOT:PSS with 680 and 1000  $\mu\text{L}$  of EG are performed and compared using Raman spectroscopy and Transmission Electron Microscope (TEM) (see Figures S6–S8 and Table S1, Supporting Information).<sup>[52–56]</sup> Distinct structural transitions between core-like (benzoid) and linear (quinoid) forms, along with variations in the area of the PSS shell on the surface of the PEDOT:PSS channel, are observed based on differing EG contents.

Figure 2a shows the schematics of potential switching mechanism of the r-OECT device for SET and RESET modes, respectively. The switching operation is fundamentally dependent on the alternation of mixed ionic-electronic conduction characteris-

tics of the PEDOT:PSS channel, which varies with the polarity of the  $V_G$ .<sup>[57]</sup> Basically, the PEDOT:PSS channel is a p-type conducting polymer that initially operates in depletion mode (normally ON). The PEDOT cations in the channel associate with PSS anions, resulting in electron loss from PEDOT, which confers p-type conductivity to the channel.<sup>[58]</sup> When the positive  $V_G$  is applied through SE ( $V_G > 0$ ), the electrolyte cations (denoted as  $[\text{EMIM}^+]$ ) are injected into the PEDOT:PSS channel while holes ( $h^+$ ) are simultaneously extracted from the channel. This results in the dedoping of the PEDOT:PSS, leading to a reduction in conductance. We defined this procedure as the SET process. Conversely, when a negative  $V_G$  is applied through the SE ( $V_G < 0$ ), the cations are diffused from the channel back to the SE, reinstating the ionic bonding between PEDOT and PSS. This leads to an enhancement in conduction. We defined this procedure as the RESET process. The degree of cation migration into the PEDOT:PSS channel is affected by factors such as channel grain size and configuration; thus, it is expected that the EG content in the PEDOT:PSS channel can serve as a switching designer for r-OECT devices. Figure 2b,c show two representative  $V_G$ – $I_{DS}$  switching characteristics (nonvolatile and volatile) for the r-OECT devices with varying EG content concentrations of 680 and 1000  $\mu\text{L}$ , respectively. Commonly, both r-OECT devices show clockwise p-type switching characteristics while gating sweep ranges of  $\pm 3.5$  V. The dynamic range (DR) of the OECT devices with EG contents of 680 and 1000  $\mu\text{L}$  is measured at  $1.12 \times 10^5$  and  $1.20 \times 10^3$ , respectively, which is several orders magnitude greater than previously reported OECT devices, as shown in Figure 2d,e.<sup>[28–33,59]</sup> Note that the DR is defined as the ratio of  $I_{ON}$  and  $I_{OFF}$  at  $V_G = 0$  V. This improved DR is associated to the utilization of a relatively larger ion of  $[\text{EMIM}]^+$  ( $\approx 0.8$  nm) in the SE, which can facilitate favorable electrostatic interactions with the PEDOT:PSS channel.<sup>[60]</sup> It results in the gradual discharge of charged ions from the PEDOT:PSS channel, which in turn expands the memory window.<sup>[61–64]</sup> Note that the OECT device did not exhibit any switching characteristics when a smaller charged ion (e.g.,  $\text{Na}^+$  of 0.19 nm) was used in a liquid electrolyte, as the ions rapidly discharged (see Figure S9, Supporting Information).<sup>[60]</sup> We also demonstrated that the DR of the 680  $\mu\text{L}$ -OECT device is maintained at a ratio of at least  $10^5$ , even after more than 60 repeated switching cycles, as shown in Figure 2f. The DR can be changed according to the magnitude of applied  $V_G$ , and the gate-leakage current ( $I_G$ ) is measured to be at least  $10^4$  orders of magnitude lower than  $I_{DS}$  under the same gate operating condition (see Figures S10 and S11, Supporting Information). Note that the  $V_{DS}$ – $I_{DS}$  output characteristics for the 680  $\mu\text{L}$ -OECT device are investigated, as shown in Figure S12 (Supporting Information). Figure 2g–i show the transient  $I_{DS}$  response of the r-OECT devices with different EG contents over time while the application of a single voltage pulse ( $V_G = 3.5$  V for 700  $\mu\text{s}$ ). The  $I_{DS}$  for the 680  $\mu\text{L}$ -OECT devices linearly decreases immediately following the application of a single  $V_G$  pulse, and this altered  $I_{DS}$  value is maintained over time, demonstrating long-term memory (LTM) (Figure 2g). This LTP can be explained by that the migrated cations, induced by the application of a positive  $V_G$  pulse, are retained within the PEDOT:PSS channel for the 680  $\mu\text{L}$ -OECT device, as illustrated in the left of Figure 2h. The retention of the PSS shell boundary in each PEDOT:PSS domain may impede the diffusion of cations back to the SE, thereby enabling the

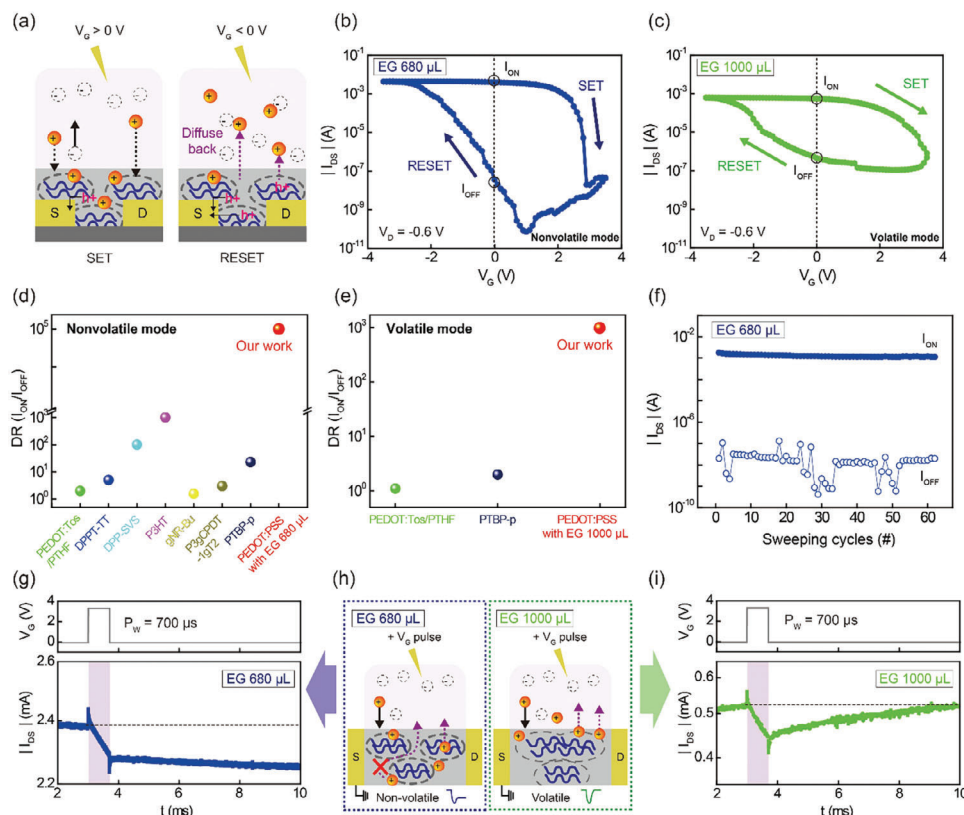


**Figure 2.** a) The schematics of potential switching mechanisms in r-OECT devices according to the polarity of the  $V_G$ . b, c)  $V_G$ - $I_{DS}$  switching characteristics (nonvolatile and volatile modes) for r-OECT devices with EG content of 680  $\mu\text{L}$  and 1000  $\mu\text{L}$ , respectively. The channel lengths are 55 and 45  $\mu\text{m}$  for EG of 680 and 1000  $\mu\text{L}$ , respectively.  $I_{ON}$  and  $I_{OFF}$  are determined at  $V_G = 0$  V. d, e) Comparisons of DR for various channels in OECT devices derived from nonvolatile and volatile sweeps, respectively. f)  $I_{ON}$  and  $I_{OFF}$  at 60 sweeping cycles for 680  $\mu\text{L}$ -OECT device. g, i) The transient  $I_{DS}$  responses for the r-OECT devices with EG content of 680 and 1000  $\mu\text{L}$  upon applying a single  $V_G$  pulse (3.5 V for  $P_W = 700$   $\mu\text{s}$ ), respectively. h) The schematics of potential switching mechanisms in r-OECT devices with EG content of 680 and 1000  $\mu\text{L}$  under an identical positive  $V_G$  pulse.

nonvolatile mode in the switching. In contrast, the  $I_{DS}$  for the 1000  $\mu\text{L}$ -OECT device linearly decreases immediately following the application of the identical single  $V_G$  pulse, and then decays spontaneously and exponentially over time, demonstrating short-term memory (STM). It is expected that incorporating an excessive quantity of EG content into the PEDOT:PSS channel would further weaken the PSS shell, resulting in the clustering of PEDOT chains into larger domains at the surface. As a result, it may obstruct the migration of cations into the deeper PEDOT:PSS channel, leading to the  $I_{DS}$  reverting to its original value, enabling the volatile mode in the switching. Larger relaxation times at longer  $P_W$  are observed due to alterations in the degree of cation migration (see Figure S13, Supporting Information). Various relaxation times could be employed to capture temporal inputs for different time periods of time-series tasks. Additional potential switching mechanism analyses for r-OECT devices with varying EG contents were performed using electrochemical impedance spectroscopy (EIS) and different cation species ( $\text{Na}^+$  and  $\text{EMIM}^+$ ) (see Figures S14 and S15, Supporting Information).<sup>[46]</sup> Note that the 0  $\mu\text{L}$ -OECT device exhibits a comparable p-type switching curve with marginally reduced conductance; however, it shows a spike and recovery pattern over time following the application of a same  $V_G$  pulse ( $V_G = 3.5$  V for 700  $\mu\text{s}$ ) (see Figure S16, Supporting Information).<sup>[65,66]</sup> A reduction in EG results in a diminished

domain size of the PSS chain, potentially impeding hole transport. In that case, the cation migration and diffusion process at the interface may occur more rapidly than hole transport across the PEDOT:PSS domains, leading to the  $I_{DS}$  transient spike behavior.

Figure 3a–c show the essential nonvolatile synaptic functions for the selected 680  $\mu\text{L}$ -OECT devices, which can be utilized as a readout layer for the physical RC. Figure 3a shows the transient  $I_{DS}$  response of the 680  $\mu\text{L}$ -OECT device over time while the application of two continuous pulses ( $V_G = 3.5$  V for  $P_W = 700$   $\mu\text{s}$ ) with an  $\Delta t$  of 400  $\mu\text{s}$ , which is analogous to the paired pulse depression (PPD) of the biological synapse.<sup>[67]</sup> Following the application of two voltage pulses, the decreased  $I_{DS}$  remains stable at its altered value over time, indicating LTM functionality. It is observed that the reduction ratio ( $\Delta_2$ ) in  $I_{DS}$  after the second pulse is slightly smaller compared to the  $\Delta_1$  after first one. We speculated that this occurs due to a reduction in the permissible area for cation migration at the channel surface following the initial input. To enhance the weight updating capability of the readout layer for learning process, each device node should possess a robust and gradual long-term depression (LTD) and long-term potentiation (LTP) with a high DR, which can be reconfigured through the application of pulse sequences. Figure 3b shows the gradual LTP and LTD function of the  $I_{DS}$  for the 680  $\mu\text{L}$ -OECT device at

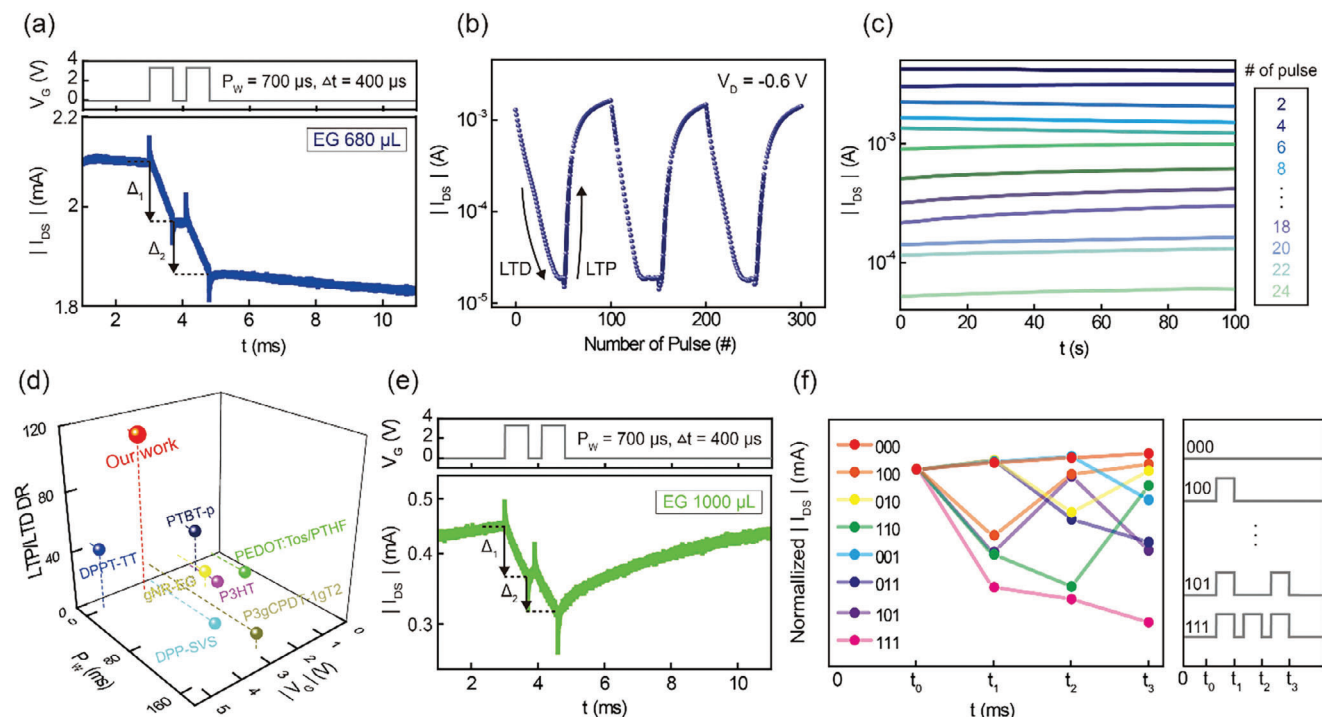


**Figure 3.** a) Transient  $I_{DS}$  response for the 680  $\mu\text{L}$ -OECT device during applying two  $V_G$  pulses (3.5 V,  $P_W = 700 \mu\text{s}$ ,  $\Delta t = 400 \mu\text{s}$ ). b) Repeated LTD and LTP function of  $I_{DS}$  for the 680  $\mu\text{L}$ -OECT device controlled by the input pulse trains ( $V_G = \pm 3.5$  V for 700  $\mu\text{s}$ ) with  $\Delta t$  of 400  $\mu\text{s}$ . c) Retention test of 12  $I_{DS}$  levels made by different numbers of  $V_G$  pulses from 2 to 24 for the 680  $\mu\text{L}$ -OECT device. d) Comparison of DR (LTP/LTD) for various channels in the OECTs as functions of  $P_W$  and  $V_G$ . e) Transient  $I_{DS}$  response for the 1000  $\mu\text{L}$ -OECT device during applying two  $V_G$  pulses (3.5 V,  $P_W = 700 \mu\text{s}$ ,  $\Delta t = 400 \mu\text{s}$ ). f) Change in physical reservoir states of 1000  $\mu\text{L}$ -OECT device at the  $V_G = 0$  V per timestep ( $t_0$ – $t_3$ ) and 3-bit binary inputs from [000] to [111].

different polarities of input pulse trains ( $V_G = \pm 3.5$  V for 700  $\mu\text{s}$ ) with the  $\Delta t$  of 400  $\mu\text{s}$ . The number of switching states for LTP or LTD functions is measured to be 50, respectively, and they can be further increased to 100 according to the number of input pulses (see Figure S17, Supporting Information). Similar LTP and LTD functions are observed in the OECT devices with different EG contents (300 and 800  $\mu\text{L}$ ) (see Figure S18, Supporting Information). Additionally, the  $I_{DS}$  modified by the  $V_G$  pulses is robustly retained, as shown in Figure 3c. The  $I_{DS}$  ratio (or DR) between the highest LTP and the lowest LTD (i.e., DR for LTP/LTD) is found to be  $\approx 1.1 \times 10^2$ , which is much higher among previously reported OECT devices,<sup>[28–33,59]</sup> as shown in Figure 3d. This high DR and large number of states in the LTP and LTD functions can offer a wide synaptic weight range and precise weight modification in response to various input signals, allowing the ANNs to learn and recognize a broader range of patterns. Figure 3e,f shows the essential volatile synaptic functions for the 1000  $\mu\text{L}$ -OECT devices, which can be utilized as a reservoir layer for the physical RC. In contrast to the 680  $\mu\text{L}$ -OECT devices, the decreased  $I_{DS}$  after the application of two  $V_G$  pulses reverted to its original value over time, indicating STP functionality (Figure 3e). Similarly, the  $\Delta_2$  in  $I_{DS}$  is slightly smaller compared to the  $\Delta_1$ . However, the  $\Delta_2/\Delta_1$  for the 1000  $\mu\text{L}$ -OECT device is lower than that for the 680  $\mu\text{L}$ -OECT one. The reason can be explained that the entangled PEDOT chain, due to the excessive EG content, may impede cation migration from the SE. This STP functionality enables the extraction of reservoir states in response to various tem-

poral voltage inputs. Figure 3f shows the change of the reservoir states (i.e., normalized  $I_{DS}$  responses) of the 1000  $\mu\text{L}$ -OECT device corresponding to each time steps ( $t_0$ – $t_3$ ) with  $\Delta t$  of 400  $\mu\text{s}$  depending on a voltage pulse sequence. 3-bit binary inputs from [000] to [111] are sequentially applied, as shown in the right of Figure 3f. Note that [000] indicates no voltage pulses are applied, while [111] indicates that three voltage pulses (3.5 V for 700  $\mu\text{s}$ ) with  $\Delta t$  of 400  $\mu\text{s}$  are sequentially applied. With these pulse configurations, eight reservoir states are distinguished at  $t_3$  in an acceptable range. In addition, the PPD index under different pulse intervals ( $\Delta t$ ) from 50 to 700  $\mu\text{s}$  at a fixed  $V_G = 3.5$  V is investigated (see Figure S19, Supporting Information). As the  $\Delta t$  increases, the PPD index is nonlinearly increased due to the diminishing effect of the second pulse on the current, which causes  $A_1$  and  $A_2$  to gradually become similar in magnitude. Note that  $A_1 = \Delta_1$  and  $A_2 = \Delta_1 + \Delta_2$ .

Based on these two synaptic switching modes (STP and LTP/LTD) with high DRs in the r-OECTs devices, it is feasible to design a fully integrated physical RC system and successfully execute the recognition and analysis of a variety of time-series information. Classifying human behavioral patterns, one of the representative forms of time-series data, has significant potential for applications such as analyzing personal habits and health conditions to provide personalized medical and service solutions, as well as enhancing user experiences in automated environments. In this context, we have performed classification of three human activities—jogging (J), brushing teeth (B), and folding



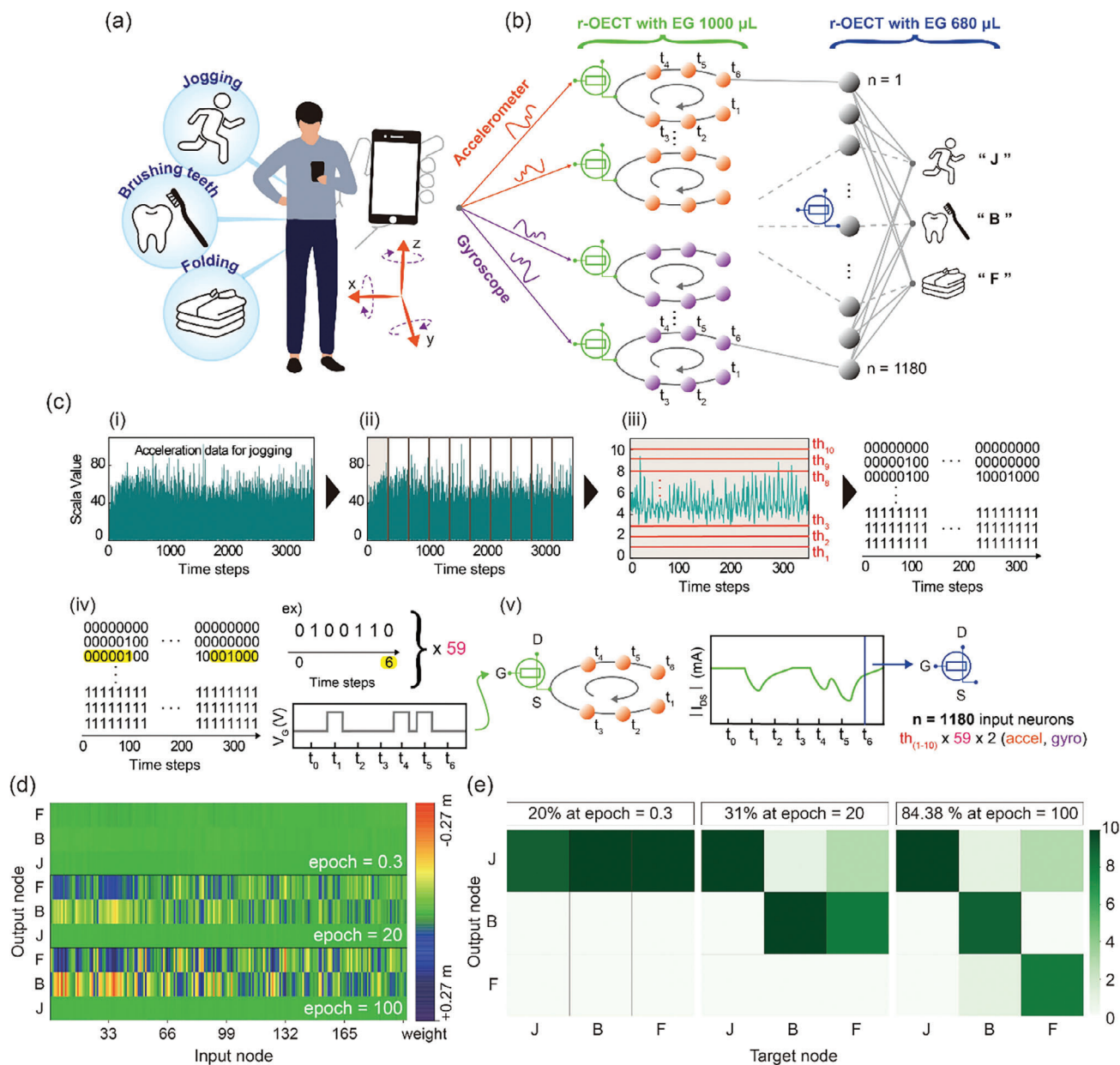


**Figure 4.** a) Schematics of three human activities detected by accelerometer and gyroscope sensor collected from smartphones: (J) jogging, (B) brushing teeth, and (F) folding clothes. b) Schematics of a fully r-OECT physical reservoir computing system comprising of the input, reservoir, and readout layers for recognizing three activities. c) An illustration of the process of preprocessing the raw jogging data from the accelerometer sensor and encoding it for the reservoir layers. d) The contour plots of the updated synaptic weights for input (1-200) and output nodes for J, B, and F activities. e) Confusion matrix and classification accuracy for three human activities (J, B, and F) across three epoch states.

clothes (F)—using our r-OECT device framework, as shown in Figure 4a,b. We used accelerometer and gyroscope sensor data collected from smartphones during three activities (see Figure S20, Supporting Information).<sup>[68]</sup> Note that 51 participants performed these activities, and they are sourced from the biometrics dataset of the WISDM (Wireless Sensor Data Mining) Lab.<sup>[68]</sup> Note that the original WISDM biometrics dataset included 18 different human activities collected from accelerometer and gyroscope sensor, which were broadly categorized into hand-oriented activities and non-hand-oriented activities. Among the non-hand-

oriented activities, jogging was selected as a representative example, while brushing teeth was chosen as a representative activity involving hand usage. Additionally, to evaluate the system's ability to distinguish between similar actions within the same category, folding clothes was included as an additional hand-oriented activity. As shown in Figure 4b, the preprocessed acceleration and gyroscope data serve as gate inputs for time-delayed reservoir layers (from  $t_1$  to  $t_6$ ) that are composed of the 1000  $\mu\text{L}$ -OECT devices. Note that  $t_0$  is the starting point and excluded in this figure. In these multiple layers, it is assumed that the final reservoir state

at each layer is determined at  $t_6$ , and then fed as each input node (the gate line) of the 680  $\mu\text{L}$ -OECD devices. The fully-connected network based on the 680  $\mu\text{L}$ -OECD devices conducts the updating process of the synaptic weight through the backpropagation process during training to classify the three activities: jogging (J), brushing teeth (B), and folding clothes (F). Detailed learning and recognition simulation are explained in Note S1 (Supporting information). Figure 4c shows an example of preprocessing the raw J data from the accelerometer sensor and encoding this data to the reservoir layers. The i) of Figure 4c shows the raw data of J for one participant before being fed to input layers. Each data is represented by a scalar value that denotes the norms of acceleration and angular velocity vectors for the time steps of 3540. In order to extract the common features while minimizing noise, a difference-based preprocessing step is applied, followed by calculating the absolute differences between consecutive values and averaging them. The resulting data are divided into 10 segments, each containing the time steps of 354, as shown in ii) of Figure 4c. These data are then converted into binary format based on whether each scalar value exceeds one of the arbitrarily set 10 thresholds ( $th_1$  to  $th_{10}$ ) ( $= 1$ ) or not ( $= 0$ ), producing binary data with the same number of time steps, as shown in iii) of Figure 4c. In step iv), the values from  $th_1$  to  $th_{10}$  for this selected time steps are masked into 59 data points with time steps of 6 each. For example, binary data "010 0110" is converted into a  $V_G$  input pulse for the 1000  $\mu\text{L}$ -OECD, where "0" corresponds to (0V,  $P_W = 700 \mu\text{s}$ ) and "1" corresponds to (3.5V,  $P_W = 700 \mu\text{s}$ ). These pulses are sequentially applied from  $t_0$  to  $t_6$ . The total time length from  $t_0$  to  $t_6$  is set to 4.9 ms considering the current relaxation time after pulse application. With these  $V_G$  input streams, the time-delayed reservoir layer generates the transient  $I_{DS}$  values, as shown in (v) of Figure 4c. The final  $I_{DS}$  value at  $t_6$  is then amplified and mapped one-to-one to the input layer of the 680  $\mu\text{L}$ -OECD devices (i.e., synaptic node in the ANNs) in the form of voltage signal. Note that the total input number is 1180, derived by multiplying the 59 reservoir states from 10 thresholds by the 2 data sources (accel. and gyro.). This process is repeated in the remaining time steps (from 354 to 3540) of (ii) of Figure 4c. Other accelerometer and gyroscope data for three activities are identically processed (see an example of preprocessing the raw J data from the gyroscope sensor and encoding this data to the reservoir layers in Figure S21, Supporting information). In the fully-connected network based on the 680  $\mu\text{L}$ -OECD devices, each synaptic weight is updated by minimizing errors using LTD/LTP functions fitted to 100 states until the conductance converges (see Figure S17, Supporting information). Figure 4d shows the contour plots of the updated synaptic weights for input and output nodes for J, B, and F activities when the number of epochs is 0.3, 20, and 100 at the limited input nodes of 200. The updated synaptic weight for 201–1180 input nodes is displayed in Figure S22 (Supporting Information). The synaptic weights are properly updated and converge with the increase in the number of epochs, suggesting that the updating process is successfully executed. Figure 4e shows the confusion matrix for the classification simulation of the three activities and the recognition accuracies at different number of epochs (0.3, 20, and 100), achieving an accuracy of  $\sim 84.38\%$ . This result demonstrates that the fully integrated r-OECDs-based physical RC could effectively recognize and analyze a diverse array of human behavioral patterns by utilizing the two

synaptic switching modes (STP and LTP/LTD) with high DRs. Note that we also assessed the recognition performance of the MNIST dataset and conducted a comparison with other OECD devices, resulting in an accuracy of 94.16% (see Figure S23 and Table S2, Supporting Information).<sup>[28–33,59,69]</sup>

### 3. Conclusion

We successfully demonstrated the fabrication and characterization of r-OECDs with dual switching modes and high DRs for fully integrated physical RC. By adjusting the EG contents in the PEDOT:PSS channel, the r-OECDs achieved nonvolatile and volatile essential synaptic functionalities, enabling them to function as both the reservoir and readout layers in the physical RC system. The nonvolatile mode, achieved with an EG content of 680  $\mu\text{L}$ , exhibited LTM behavior and the reliable transition between LTP and LTD with high DR, essential for weight updates in the readout layer. In contrast, the volatile mode, achieved with an EG content of 1000  $\mu\text{L}$ , demonstrated STM behavior, facilitating the extraction of dynamic reservoir states for processing temporal information. The r-OECDs containing 680 and 1000  $\mu\text{L}$  of EG exhibited remarkable DRs of  $1.12 \times 10^5$  in nonvolatile mode and  $1.20 \times 10^3$  in volatile mode, respectively, indicating a substantial enhancement compared to earlier reported OECDs. Attaining this high DRs in both modes can improve the capacity to capture a broader spectrum of input signal variations and execute more complex nonlinear transformations within the reservoir layer, in addition to augmenting the reconfigurability of the readout layer, which improving the accuracy and efficiency of the physical RC system. The r-OECDs-based physical RC system was successfully employed to classify human activities, such as jogging, brushing teeth, and folding clothes, using accelerometer and gyroscope data, achieving high classification accuracy of 84.38%. The successful implementation of both reservoir and readout layers using r-OECDs, as presented in this study, marks a significant step toward fully integrated physical RC systems. The devices' ability to achieve a wide dynamic range across both layers, facilitated by a novel design approach, highlights their capability to perform the complex computations required for physical RC system. These findings pave the way for the development of more compact, energy-efficient, and adaptable RC systems based on r-OECD technology.

### 4. Experimental Section

**Material Preparation:** The following materials were used in the experiments: N-isopropylacrylamide (monomer; 99.0%, Sigma-Aldrich), N,N'-methylenebisacrylamide (crosslinker; 99.0% Sigma-Aldrich), 2-hydroxy-4'-(2-hydroxyethoxy)-2-methylpropiophenone (initiator; 98.0%, Sigma-Aldrich), 1-ethyl-3-methylimidazolium ethyl sulfate (ionic liquid; 95.0%, Sigma-Aldrich), (3-Glycidyloxypropyl)trimethoxysilane (GOPS; 98.0%, Sigma-Aldrich), ethylene glycol (99.8%, Sigma-Aldrich), 4-Dodecylbenzenesulfonic acid (DBSA; 95.0%, Sigma-Aldrich), and PEDOT:PSS (Clevios PH1000, Heraeus Deutschland GmbH & Co. KG).

**Fabrication of r-OECD Device:** As source (S) and drain (D) electrodes, Au/Al (30/3 nm) metal were patterned onto a  $1.5 \times 2.0 \text{ cm}^2$   $\text{SiO}_2$  (285 nm)/ $p^{++}$  Si substrate via photolithography after the typical cleaning process, and then deposited them using a thermal evaporator. (see (i) of Figure 1b) The channel lengths between the S and D electrodes used in this study are 45 and 55  $\mu\text{m}$ . To define each channel area of the r-OECD devices and expose contact pads, a  $\text{SiO}_2$  insulating layer (70 nm) was deposited



via RF sputtering under conditions of  $\text{CF}_4$  at 40 sccm and  $\text{O}_2$  at 4 sccm, followed by a reactive ion etching (RIE) process to selectively remove  $\text{SiO}_2$  from the channel and contact pad regions after the photolithography process. (see (ii) of Figure 1b) This process establishes a predetermined channel width of 400  $\mu\text{m}$ . Prior to the spin-coating process of the PEDOT:PSS channel, a 3 min-treatment of  $\text{O}_2$  plasma cleaning is applied to the device to create the well-defined coated film. For the channel layer, 680 and 1000  $\mu\text{L}$  of EG, along with 0.1 wt.% DBSA and 1 wt.% GOPS, were added to 5 mL of PEDOT:PSS solution and synthesized by stirring for 17 m, respectively. (see Figure S1, Supporting Information) These PEDOT:PSS solutions modified by different EG contents were spin-coated at 500 rpm for 5 s and 2000 rpm for 46 s, subsequently heat-treated at 130  $^\circ\text{C}$  for 1 h. (see (ii) of Figure 1b) The thickness of the coated-PEDOT:PSS film was measured to be  $\approx 100$  nm by Dektak-XT stylus profilometer. (see Figure S3, Supporting Information) After then, the patterned photoresist was smoothly lifted off using acetone for 10 min. For the preparation of the SE, the precursor solution was mixed with 750.0 mg monomer, 20.0 mg crosslinker, 200.0 mg initiator, and 1.5 mL ionic liquid in 1.0 mL deionized water, then stirred at 550 rpm overnight. (see Figure S2, Supporting Information) The SE precursor solution was selectively dropped onto the channel area by a syringe, then exposed to UV light for 25 s for its solidification. (see (iii) of Figure 1b) With this process, the r-OECT devices were fabricated. (see (iv) of Figure 1b). All fabrication processes were carried out under ambient conditions at room temperature and atmospheric pressure.

**Electrical and Material Characterization:** All electrical measurements of the r-OECT devices were carried out in vacuum conditions using a Keithley 4200 semiconductor characterization system. The S electrode was grounded, and the Au-probe tip was carefully placed on the SE to serve as a gate electrode. The surface morphology and RMS of the coated PEDOT:PSS channel with the EG contents of 680 and 1000  $\mu\text{L}$  were investigated by non-contact mode of AFM (ParkSystems, NX-10).

## Supporting Information

Supporting Information is available from the Wiley Online Library or from the author.

## Acknowledgements

C.H., M.K., and S.J.P. contributed equally to this work. This study was supported by the National R&D Program administered by the National Research Foundation of Korea (NRF) of the Korea government (Grant Nos. RS2023-00220077, 2022M3H4A1A0100952621, 2022R1A2C1005421, RS-2024-00451891, RS-2024-00439520, and RS-2024-00407271), Korea Institute of Science and Technology (KIST) Institutional Program (2E33181-24-081), Korea University-Korea Institute of Science and Technology (KU-KIST) Graduate School Program of Korea University, and Korea University Research Grant.

## Conflict of Interest

The authors declare no conflict of interest.

## Data Availability Statement

The data that support the findings of this study are available from the corresponding author upon reasonable request.

## Keywords

dynamic range, organic electrochemical transistor, physical reservoir computing, reconfigurable

Received: December 4, 2024

Revised: January 24, 2025

Published online:

- [1] T. W. Liao, *Pattern Recogn.* **2005**, *38*, 1857.
- [2] S. Kaushik, A. Choudhury, P. K. Sheron, N. Dasgupta, S. Natarajan, L. A. Pickett, V. Dutt, *Front. Big. Data.* **2020**, *3*, 4.
- [3] T.-c. Fu, F.-I. Chung, R. Luk, C.-m. Ng, *Eng. Appl. Artif. Intell.* **2008**, *21*, 277.
- [4] C. J. Taylor, D. J. Pedregal, P. C. Young, W. Tych, *Environ. Model. Software.* **2007**, *22*, 797.
- [5] J. F. Torres, D. Hadjout, A. Sebaa, F. Martínez-Álvarez, A. Troncoso, *Big Data.* **2021**, *9*, 3.
- [6] A. Dridi, H. I. Khedher, H. Mounsla, H. Affi, presented at *2020 International Wireless Communications and Mobile Computing (IWCMC)*, IEEE, Piscataway, NJ **2020**.
- [7] A. Sherstinsky, presented at *Critiquing and Correcting Trends in Machine Learning Workshop at Neural Information Processing Systems*, Montréal, Canada **2018**.
- [8] R. C. Staudemeyer, E. R. Morris, arXiv preprint arXiv:1909.09586 **2019**.
- [9] M. Jogin, M. Madhulika, G. Divya, R. Meghana, S. Apoorva, presented at *2018 3rd IEEE International Conference on Recent Trends in Electronics, Information & Communication Technology (RTEICT)*, IEEE, Piscataway, NJ **2018**.
- [10] I. D. Mienye, T. G. Swart, G. Obaido, *Information* **2024**, *15*, 517.
- [11] J. Moon, W. Ma, J. H. Shin, F. Cai, C. Du, S. H. Lee, W. D. Lu, *Nat. Electron.* **2019**, *2*, 480.
- [12] G. Milano, G. Pedretti, K. Montano, S. Ricci, S. Hashemkhani, L. Boarino, D. Ielmini, C. Ricciardi, *Nat. Mater.* **2022**, *21*, 195.
- [13] G. Tanaka, T. Yamane, J. B. Heroux, R. Nakane, N. Kanazawa, S. Takeda, H. Numata, D. Nakano, A. Hirose, *Neural Network.* **2019**, *115*, 100.
- [14] Z. Zhang, X. Zhao, X. Zhang, X. Hou, X. Ma, S. Tang, Y. Zhang, G. Xu, Q. Liu, S. Long, *Nat. Commun.* **2022**, *13*, 6590.
- [15] D. Ju, M. Noh, G. Kim, Y. Park, S. Lee, S. Kim, *ACS Appl. Mater. Interfaces* **2024**, *16*, 66250.
- [16] M. Ismail, M. Rasheed, Y. Park, J. Lee, C. Mahata, S. Kim, *Nanoscale* **2024**, *17*, 361.
- [17] Y. Zhong, J. Tang, X. Li, B. Gao, H. Qian, H. Wu, *Nat. Commun.* **2021**, *12*, 408.
- [18] Y. Shi, N. T. Duong, Y. C. Chien, S. Li, H. Xiang, H. Zheng, K. W. Ang, *Adv. Funct. Mater.* **2024**, *34*, 34.
- [19] S. Choi, J. Shin, G. Park, J. S. Eo, J. Jang, J. J. Yang, G. Wang, *Nat. Commun.* **2024**, *15*, 2044.
- [20] X. Liang, J. Tang, Y. Zhong, B. Gao, H. Qian, H. Wu, *Nat. Electron.* **2024**, *7*, 193.
- [21] Y. Zhong, J. Tang, X. Li, X. Liang, Z. Liu, Y. Li, Y. Xi, P. Yao, Z. Hao, B. Gao, H. Qian, H. Wu, *Nat. Electron.* **2022**, *5*, 672.
- [22] D. Ohayon, V. Druet, S. Inal, *Chem. Soc. Rev.* **2023**, *52*, 1001.
- [23] J. Rivnay, S. Inal, A. Salleo, R. M. Owens, M. Berggren, G. G. Malliaras, *Nat. Rev. Mater.* **2018**, *3*, 1.
- [24] B. D. Paulsen, K. Tybrandt, E. Stavrinidou, J. Rivnay, *Nat. Mater.* **2020**, *19*, 13.
- [25] R. Bhunia, E. K. Boahen, D. J. Kim, H. Oh, Z. Kong, D. H. Kim, *J. Mater. Chem. C.* **2023**, *11*, 7485.
- [26] M. Cucchi, C. Gruener, L. Petruskas, P. Steiner, H. Tseng, A. Fischer, B. Penkovsky, C. Matthus, P. Birkholz, H. Kleemann, K. Leo, *Sci. Adv.* **2021**, *7*, eabh0693.
- [27] D. Liu, X. Tian, J. Bai, S. Wang, S. Dai, Y. Wang, Z. Wang, S. Zhang, *Nat. Electron.* **2024**, *7*, 1176.
- [28] N. Kim, G.-T. Go, H.-L. Park, Y. Ahn, J. Kim, Y. Lee, D.-G. Seo, W. Lee, Y.-H. Kim, H. Yang, T.-W. Lee, *Adv. Intell. Syst.* **2023**, *5*, 2300016.
- [29] R. Liu, X. Zhu, J. Duan, J. Chen, Z. Xie, C. Chen, X. Xie, Y. Zhang, W. Yue, *Angew. Chem. Int. Ed. Engl.* **2024**, *63*, 202315537.
- [30] Y. He, Z. Ge, Z. Li, Z. Li, R. Liu, L. Zhang, L. Lan, W. Yue, Z. Xie, *Adv. Funct. Mater.* **2024**, 2415595.

- [31] Y. Yin, S. Wang, R. Weng, N. Xiao, J. Deng, Q. Wang, Z. Wang, P. K. L. Chan, *Small Sci.* **2024**, 5, 2400415.
- [32] S. Wang, X. Chen, C. Zhao, Y. Kong, B. Lin, Y. Wu, Z. Bi, Z. Xuan, T. Li, Y. Li, W. Zhang, E. Ma, Z. Wang, W. Ma, *Nat. Electron.* **2023**, 6, 281.
- [33] X. Liu, S. Dai, W. Zhao, J. Zhang, Z. Guo, Y. Wu, Y. Xu, T. Sun, L. Li, P. Guo, J. Yang, H. Hu, J. Zhou, P. Zhou, J. Huang, *Adv. Mater.* **2024**, 36, 2312473.
- [34] C. Du, F. Cai, M. A. Zidan, W. Ma, S. H. Lee, W. D. Lu, *Nat. Commun.* **2017**, 8, 2204.
- [35] K. Kim, M. S. Song, H. Hwang, S. Hwang, H. Kim, *Front. Neurosci.* **2024**, 18, 1279708.
- [36] R. Islam, H. T. Li, P. Y. Chen, W. E. Wan, H. Y. Chen, B. Gao, H. Q. Wu, S. M. Yu, K. Saraswat, H. S. P. Wong, *J. Phys. D: Appl. Phys.* **2019**, 52, 113001.
- [37] L. Wang, Y. Zhang, Z. Guo, Z. Wu, X. Chen, S. Du, *Micromachines* **2022**, 13, 1700.
- [38] Y. Zhao, W. Duan, C. Wang, S. Xiao, Y. Li, Y. Li, J. An, H. Li, *Front. Neurosci.* **2023**, 17, 1177118.
- [39] S. Lee, Y. Park, S. Jung, S. Kim, *J. Chem. Phys.* **2023**, 159, 234701.
- [40] R. Gangopadhyay, B. Das, M. R. Molla, *RSC Adv.* **2014**, 4, 43912.
- [41] S. Yamamoto, *Flex. Print. Electron.* **2024**, 9, 013001.
- [42] A. Weissbach, L. M. Bongartz, M. Cucchi, H. Tseng, K. Leo, H. Kleemann, *J. Mater. Chem. C* **2022**, 10, 2656.
- [43] C. S. Suchand Sangeeth, M. Jaiswal, R. Menon, *J. Phys. Condens. Matter.* **2009**, 21, 072101.
- [44] A. M. Nardes, R. A. J. Janssen, M. Kemerink, *Adv. Funct. Mater.* **2008**, 18, 865.
- [45] E. Hosseini, V. Ozhukil Kollath, K. Karan, *J. Mater. Chem. C* **2020**, 8, 3982.
- [46] A. L. Oechsle, T. Schoner, L. Deville, T. Xiao, T. Tian, A. Vagias, S. Bernstorff, P. Muller-Buschbaum, *ACS Appl. Mater. Interfaces* **2023**, 15, 47682.
- [47] T. Murakami, Y. Mori, H. Okuzaki, *Trans. Mater. Res. Soc. Jpn.* **2011**, 36, 165.
- [48] Y.-J. Lin, W.-S. Ni, J.-Y. Lee, *J. Appl. Phys.* **2015**, 117.
- [49] A. Srivastava, R. K. Sharma, D. Sharma, J. S. Tawale, V. V. Agrawal, S. K. Srivastava, *Opt. Mater.* **2022**, 134, 112922.
- [50] Q. Wei, M. Mukaida, Y. Naitoh, T. Ishida, *Adv. Mater.* **2013**, 25, 2831.
- [51] H.-Q. Cui, R.-X. Peng, W. Song, J.-F. Zhang, J.-M. Huang, L.-Q. Zhu, Z.-Y. Ge, *Chin. J. Polym. Sci.* **2019**, 37, 760.
- [52] Y. Huang, Y. Zeng, Z. Zhang, X. Guo, M. Liao, C. Shou, S. Huang, B. Yan, J. Ye, *Sol. Energy Mater. Sol. Cells* **2019**, 192, 154.
- [53] J. Liu, J. Niu, D. Yang, M. Yan, J. Sha, *Phys. E* **2004**, 23, 221.
- [54] M. Kong, M. Garriga, J. S. Reparaz, M. I. Alonso, *ACS Omega* **2022**, 7, 39429.
- [55] S. Garreau, G. Louarn, J. Buisson, G. Froyer, S. Lefrant, *Macromolecules* **1999**, 32, 6807.
- [56] F. Tran-Van, S. Garreau, G. Louarn, G. Froyer, C. Chevrot, *J. Mater. Chem.* **2001**, 11, 1378.
- [57] C. Zhao, J. Yang, W. Ma, *Nanomicro Lett.* **2024**, 16, 233.
- [58] J. E. Tyrrell, M. G. Boutelle, A. J. Campbell, *Adv. Funct. Mater.* **2021**, 31, 2007086.
- [59] Y. Peng, L. Gao, C. Liu, J. Deng, M. Xie, L. Bai, G. Wang, Y. Cheng, W. Huang, J. Yu, *Nano Res.* **2023**, 16, 10206.
- [60] A. Elbourne, S. McDonald, K. Voichovsky, F. Endres, G. G. Warr, R. Atkin, *ACS Nano* **2015**, 9, 7608.
- [61] J. Bisquert, *J. Phys. Chem. Lett.* **2023**, 14, 10951.
- [62] S. Yamamoto, A. G. Polyavas, S. Han, G. G. Malliaras, *Adv. Electron. Mater.* **2022**, 8, 4.
- [63] Y. Li, Y. Pang, L. Wang, Q. Li, B. Liu, J. Li, S. Liu, Q. Zhao, *Adv. Mater.* **2024**, 36, 2310973.
- [64] L. M. Bongartz, A. Weissbach, M. Cucchi, K. Leo, H. Kleemann, In *2022 IEEE International Conference on Flexible and Printable Sensors and Systems (FLEPS)*, IEEE, Piscataway, NJ **2022**.
- [65] J. T. Friedlein, R. R. McLeod, J. Rivnay, *Org. Electron.* **2018**, 63, 398.
- [66] P. R. Paudel, M. Skowrons, D. Dahal, R. K. Radha Krishnan, B. Lüssem, *Adv. Theory Simul.* **2022**, 5, 2100563.
- [67] S. Choi, J. Yang, G. Wang, *Adv. Mater.* **2020**, 32, 2004659.
- [68] G. M. Weiss, *UCI ML Repository: WISDM Smartphone and Smartwatch Activity and Biometrics Dataset Data Set* **2019**, 7, 133190.
- [69] Y. Xu, Y. Shi, C. Qian, P. Xie, C. Jin, X. Shi, G. Zhang, W. Liu, C. Wan, J. C. Ho, *Nano Lett.* **2023**, 23, 5264.